

Crystal and magnetic structure of $\text{La}_{1-x}\text{Ca}_x\text{MnO}_3$ compound ($0.11 \leq x \leq 0.175$)M. Pissas¹, I. Margiakaki², G. Papavassiliou¹, D. Stamosopoulos¹, and D. Argyriou³¹Institute of Materials Science, National Center for Scientific Research, Demokritos, 15310 Ag. Paraskevi, Athens, Greece²European Synchrotron Radiation Facility (ESRF), 38043 Grenoble, Cedex 9, France³Berlin Neutron Scattering Center, Hahn-Meitner-Institut, Glienicker Str. 100 D-14109, Berlin, Germany

(Dated: May 23, 2019)

We studied the crystal and magnetic structure of the $\text{La}_{1-x}\text{Ca}_x\text{MnO}_3$ compound for $0.11 \leq x \leq 0.175$ using stoichiometric samples. For $x < 0.13$ the system's ground state is insulating canted antiferromagnetic. For $0.13 \leq x \leq 0.175$ below the Jahn-Teller transition temperature (T_{JT}) the crystal structure undergoes a monoclinic distortion. The crystal structure can be described with $P2_1/c$ space group which perm its two Mn sites. The unit cell strain parameter $s = 2(a - c)/(a + c)$ increases for $T < T_{JT}$, taking the maximum value at the Curie point, and then decreases. Below $T_{Mn} = 60$ K s abruptly changes slope and finally approaches $T = 0$ K with nearly zero slope. The change of s at $T_{Mn} = 60$ K is connected to a characteristic feature in the magnetic measurements. As x increases towards the ferromagnetic metallic boundary, although s is reduced appreciably, the monoclinic structure is preserved. The monoclinic structure is discussed with relation to the orbital ordering, which can produce the ferromagnetic insulating ground state. We also studied samples that were prepared in air atmosphere. This category of samples shows ferromagnetic insulating behavior without following the particular variation of the s parameter. The crystal structure of these samples is related to the so-called O ($c > a > b = \sqrt{2}$) structure.

PACS numbers: 75.47.Lx, 75.47.GK, 75.25.+z, 75.30Cv

I. INTRODUCTION

The nature of the ferromagnetic insulating state (FM I) in lightly doped $\text{La}_{1-x}\text{A}_x\text{MnO}_3$ ($\text{A} = \text{Sr}, \text{Ca}, x = 0.1-0.2$) rare-earth manganite perovskites continues to offer significant challenges in our understanding of the physical properties of these materials. Typically, insulating compounds of this category are antiferromagnetic, and ferromagnetism is associated with a metallic behavior that arises from doping and double exchange. The FM I state can be realized with a certain orbital ordering favorable for ferromagnetism.¹ In the intermediate doping levels ($x = 0.23-0.4$) where the ferromagnetic metallic (FM M) state is observed the double-exchange mechanism is able to explain some of the experimental results. Despite of the numerous studies concerning the FM I phase of $\text{La}_{1-x}\text{Sr}_x\text{MnO}_3$ compound, for the Ca case only a few exist. Furthermore, the tendency of this system in particular to produce cation deficient samples complicates the situation. For the Sr case the $x = 0.125$ sample shows a transition to a FM M state from paramagnetic insulating state, followed by an abrupt first-order transition to the FM I phase. The FM I state coexists with a weak antiferromagnetic component with the A type magnetic structure as was found in LaMnO_3 .² In addition in some other studies^{3,4} charge or orbital ordering have been proposed to occur in the FM I state.

The manganite perovskites of interest to this work consist of a 3D network of corner-sharing BX_6 octahedra located at the nodes of a simple cubic lattice. At the center of the unit cell there is room for the A cation

which will tilt perfectly if $d_{\text{A}}/x = d_{\text{B}}/x/\sqrt{2}$. When $d_{\text{A}}/x < d_{\text{B}}/x/\sqrt{2}$ the BX_6 octahedra are tilted to fill the extra interstitial space (steric effect). The steric effect in $\text{La}_{1-x}\text{Ca}_x\text{MnO}_3$ compound leads to a lower symmetry structure with space group $Pnma$ (in comparison to the aristoype cubic perovskite $Pm\bar{3}m$ structure) which according to the Glazer's classification⁵ belongs to the

+ tilt system (adopted by GdFeO_3 and CaTiO_3 perovskites). The adoption of the GdFeO_3 tilting scheme in $\text{La}_{1-x}\text{Ca}_x\text{MnO}_3$ is due to the small radius of the La and Ca, with respect to its surrounding cage. Thus, in order that the La ion can be accommodated in the structure, the MnO_6 -octahedra tilt. Practically MnO_6 octahedra rotation is not rigid. Below a characteristic temperature the $\text{La}_{1-x}\text{Ca}_x\text{MnO}_3$ compound for $x < 0.23$ displays cooperative JT distortion arising from ordering of the e_g orbital of the Mn^{+3} ion. This structure is denoted as $P\bar{1}$ and the unit cell satisfies the inequality $a > c > b = \sqrt{2}$. For this phase, Mn^{+3} e_g orbitals are ordered in such a way so that in neighboring Mn sites the $\beta x^2 - r^2 i$ and $\beta z^2 - r^2 i$ orbitals are alternatively occupied, forming a "canted" orbital structure. This con guration does not change along b axis.

Two mechanisms have been proposed to explain the orbital ordering in degenerated transition metal orbital states. The first is related with lattice distortions⁷ and the second is a direct generalization of the usual superexchange which in the case of orbital degeneracy is present.⁸ The orbital ordering can be described by using the pseudospin-1/2, T_i operator in such a way so that the state $\uparrow\downarrow^2 = \uparrow\downarrow i$ corresponds to the orbitals

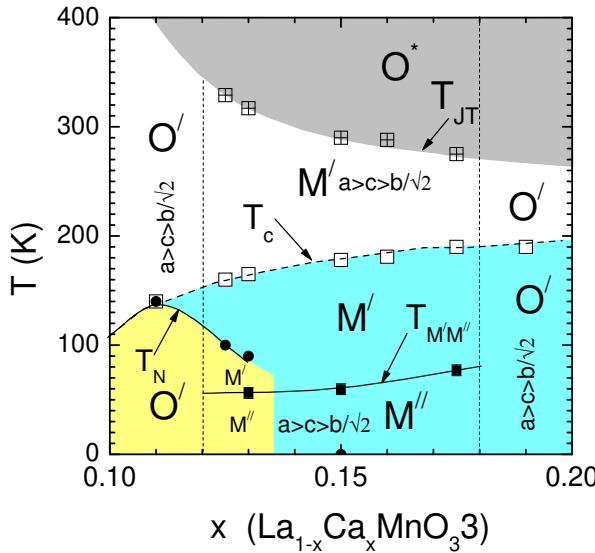


FIG. 1: Ferromagnetic insulating part of the phase diagram of $\text{La}_{1-x}\text{Ca}_x\text{MnO}_3$ compound. The light yellow region corresponds to the CAF regime, and the light blue to the FM I regime. The symbols O^* , O^- , O^{--} , M' and M'' have the following meaning: O^* orthorhombic Pnmam symmetry with $c > a > b = \sqrt{2}a$, O^- , O^{--} orthorhombic Pnmam symmetry with $a > c > b = \sqrt{2}$ and strong (intermediate) anisotropic bond lengths; and M' , M'' monoclinic $P_{21}=c$ symmetry with $a > c > b = \sqrt{2}$ and strong (intermediate) anisotropic bond lengths. The $T_{\text{M}''\text{M}''}$ is defined at the temperature where the slope of the $a(T)$ and $b(T)$ curves change slope abruptly upon heating from $T = 0$. The T_{JT} curve is defined at the temperature where the $m(T)$ curves display a jump-like or slope-change behavior. The T_c and T_N are both estimated from neutron and magnetization data.

βz^2 $r^2 i$ and βx^2 $y^2 i$, respectively. An arbitrary distortion can be described by linear superposition of the states $\mathbf{f}^z = \mathbf{j}^z - 2\mathbf{i}$, e.g. $\mathbf{j}^z = \cos(\theta/2)\mathbf{j}^x + \sin(\theta/2)\mathbf{j}^y$ where θ is an angle in the $(\mathbf{f}^z; \mathbf{T}^z)$ plane.

Finally, there is a third orthorhombic phase, O^* ($c > a > b = \sqrt{2}a$), related to orbital disordered manganites ($x > 0.23$). The O^* -structure, is pseudocubic with the Mn-O bond lengths almost equal, indicating that it lacks a clear static JT distortion. Both phases exhibit the orthorhombic Pnmam symmetry.

In this article we present a synchrotron x-ray and neutron diffraction study, using carefully prepared stoichiometric $\text{La}_{1-x}\text{Ca}_x\text{MnO}_3$ ($0.11 \leq x \leq 0.175$) samples in order to isolate the structural and magnetic features that characterize the FM I state. Our diffraction results on stoichiometric samples show that the crystal structure at FM I regime is monoclinic $P_{21}=c$. The temperature variation of the unit cell parameters is non monotonic, defining the T_{JT} and $T_{\text{M}''\text{M}''}$ temperatures. In addition, this monoclinic crystal structure permits two Mn crystallographic sites. This crystal structure is different from that of the cation deficient samples and samples that belong

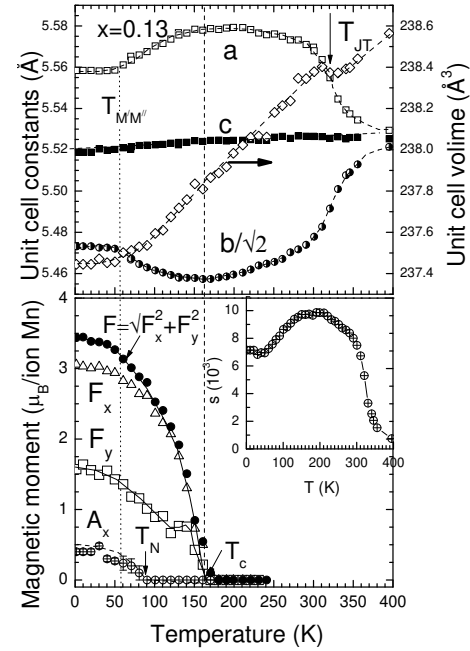


FIG. 2: (upper panel) Temperature variation of the lattice parameters and unit-cell volume for $\text{La}_{0.87}\text{Ca}_{0.13}\text{MnO}_3$ compound. (lower panel) Temperature variation of the ordered ferromagnetic and antiferromagnetic moments. The ferromagnetic components are denoted by F and the antiferromagnetic with A . The inset shows the temperature variation of the spontaneous orthorhombic strain ($s = 2(a - c)/a + c$). Lines through the experimental points are guides to the eye.

in the ferromagnetic metallic regime.

II. EXPERIMENTAL DETAILS

$\text{La}_{1-x}\text{Ca}_x\text{MnO}_3$ samples are prepared by thoroughly mixing high purity stoichiometric amounts of CaCO_3 , La_2O_3 , and MnO_2 . The mixed powders reacted in air up to 1400°C for several days with intermediate grinding. Finally the samples were slowly cooled to 250°C . These samples are cation deficient.^{9,10,11} In order to produce stoichiometric samples additional annealing in He atmosphere was applied. More specifically, in the final preparation step the samples were heated under He flow up to 1100°C for 48 h followed by rapid cooling to room temperature. It is important to stress here that in the doping range examined in this work the samples red in air in all preparation steps are not stoichiometric. Although these samples are ferromagnetic and insulating for $x < 0.2$, they do not exhibit all the features of the stoichiometric samples, especially the cooperative Jahn-Teller (JT) distortion feature for $T < T_{\text{JT}}$.

Neutron powder diffraction (NPD) data were collected on the E 6 and E 9 neutron diffractometers at the Berlin Neutron Scattering Center (BENSC), located at the Hahn-Meitner-Institut, Berlin. The neutron powder

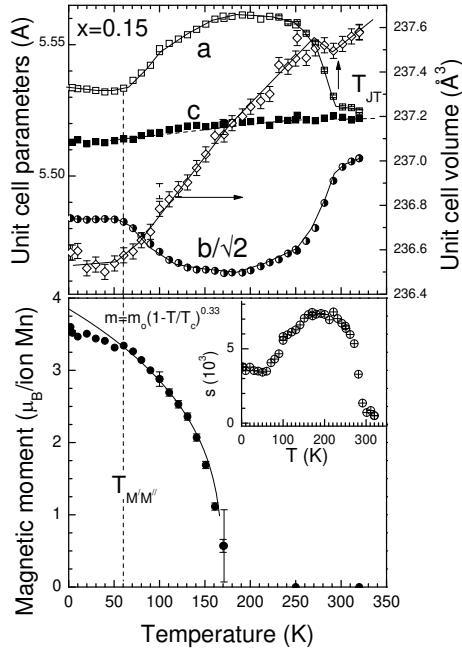


FIG . 3: (upper panel) Temperature variation of the lattice parameters and unit-cell volume for $\text{La}_{0.85}\text{Ca}_{0.15}\text{MnO}_3$ compound. Lines through the experimental points are guides to the eye. (lower panel) Temperature variation of the ordered ferromagnetic moment. The solid line is the calculated ordered moment supposing a power law. The inset shows the temperature variation of the spontaneous orthorhombic strain ($s = 2(a - c) = a + c$).

diffraction measurements on the E6 diffractometer were performed as a function of temperature at low angles using (002) reflection of pyrolytic graphite monochromator, giving a wavelength $\lambda = 2.4\text{\AA}$. For high resolution crystal structure determinations we measured NPD data using the E9 diffractometer with a wavelength of $\lambda = 1.798\text{\AA}$ ((511) reflection of a vertically bent Ge monochromator) and collimation $\theta_1 = 18^\circ$ (in pile collimator), $\theta_2 = 20^\circ$ (second collimator after monochromator), $\theta_3 = 10^\circ$ (third collimator after sample). The powdered samples were contained in a cylindrical vanadium can ($D = 8\text{ mm}$) mounted in an ILL orange cryostat.

For high resolution x-ray diffraction data we used the ID 31 high resolution powder diffraction beam line of the European Synchrotron Radiation Facility (ESRF). For our measurements we select a wavelength $\lambda = 0.50019\text{\AA}$. Nuclear and magnetic structures were determined and refined from the NPD data by using the Rietveld method with the FULLPROF suite of programs.¹² For synchrotron x-ray diffraction data, the GSAS suite was used.^{13,14} As peak shape function we used the gaussians convoluted with axial divergence asymmetry function¹⁵ for neutron data and the constant wave length profile function no 4 of the GSAS for the x-ray data. DC magnetization measurements were performed in a superconducting quantum interference device (SQUID)

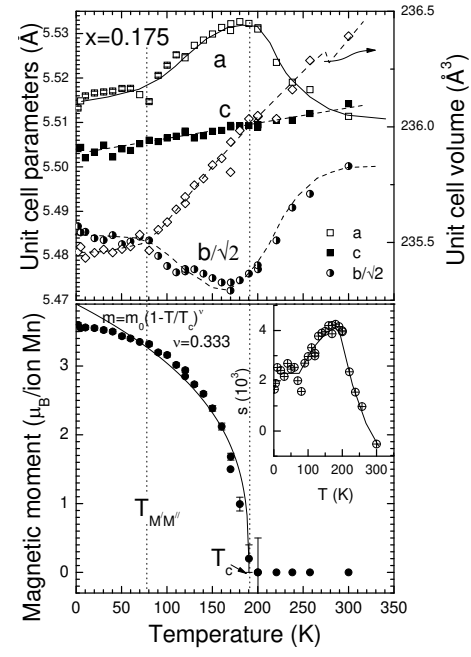


FIG . 4: (upper panel) Temperature variation of the lattice parameters and unit-cell volume for $\text{La}_{0.825}\text{Ca}_{0.175}\text{MnO}_3$ compound. Lines through the experimental points are guides to the eye. (lower panel) Temperature variation of the ordered ferromagnetic moment. The solid line is the calculated ordered moment supposing a power law. The inset shows the temperature variation of the spontaneous orthorhombic strain ($s = 2(a - c) = a + c$).

magnetometer (Quantum Design). Finally, for the ac susceptibility measurements we used a home made ac-susceptometer.

III. CRYSTAL STRUCTURE REFINEMENTS

Our structural and magnetization results on stoichiometric $\text{La}_1-x\text{Ca}_x\text{MnO}_3$, with an emphasis on the FM I regime, are summarized in Fig. 1 in the form of a phase diagram. The particular phase diagram is in good agreement with the one estimated by Biotteau et al.,¹⁶ using single crystal samples. The T_{JT} curve is defined at the temperature where the magnetization curves display a jump-like or slope-change behavior and the unit cell parameter a (b) increases (decreases) abruptly on cooling. The particular behavior of the unit cell constants resemble the situation observed in LaMnO_3 compound on cooling through the T_{JT} transition.¹⁷ Depending on x , for $T < T_{JT}$ a symmetry change from $P\text{nm}$ to $P2_1=c$ occurs. The $T_C(x)$ and $T_N(x)$ lines concern the Curie and Néel temperatures as were estimated both from neutron and magnetization data. The line $T_{MM''}(x)$ is defined at the temperature where the $a(T)$ and $b(T)$ curves display an abrupt slope change, upon heating from $T = 0$. Based on the transition lines mentioned above the phase

TABLE I: $\text{La}_1 \times \text{Ca}_x \text{MnO}_3$ ($x = 0.125$) structural parameters at several temperatures, as determined from Rietveld refinements based on neutron powder diffraction data of E9 diffraction meter ($a = 1.79784 \text{ \AA}$). The monoclinic space group $P2_1=c=P112_1=a$ (no 14, unique c -axis) was used. In this space group La, Ca O 1, O 2A and O 2B occupy the general 4e position ($x;yz$). Mn1 and Mn2 occupy the 2c ($1/2,0,0$) and 2d ($1/2,1/2,0$) positions respectively. Numbers in parentheses are statistical errors of the last significant digit.

T (K)	300	198.4	121	48	2
a (Å)	5.5754 (1)	5.5855 (1)	5.5829 (1)	5.5709 (1)	5.5697 (1)
b (Å)	7.7423 (1)	7.7213 (1)	7.7186 (1)	7.7288 (1)	7.7296 (1)
c (Å)	5.5269 (1)	5.5253 (1)	5.5234 (1)	5.5206 (1)	5.5205 (1)
(deg.)	90.125 (3)	90.130 (5)	90.127 (4)	90.106 (6)	90.107 (5)
La,Ca					
x	0.0319 (4)	0.0344 (3)	0.0348 (6)	0.0342 (3)	0.0341 (3)
y	0.2501 (8)	0.2487 (5)	0.2477 (7)	0.2479 (9)	0.2485 (8)
z	0.0058 (5)	0.0049 (4)	0.0055 (4)	0.0064 (4)	0.0061 (4)
B	0.69 (4)	0.57 (3)	0.43 (3)	0.33 (3)	0.37 (3)
Mn1	B	0.38 (7)	0.30 (6)	0.24 (6)	0.19 (5)
Mn2	B	0.38 (7)	0.30 (6)	0.24 (6)	0.19 (5)
O 1	x	0.4909 (6)	0.4898 (5)	0.4906 (5)	0.4909 (5)
	y	0.244 (1)	0.247 (1)	0.246 (1)	0.248 (1)
	z	-0.0670 (6)	-0.0679 (4)	-0.0688 (5)	-0.0687 (4)
	B	1.01 (6)	0.87 (5)	0.74 (5)	0.60 (4)
O 2A	x	0.213 (1)	0.211 (1)	0.209 (1)	0.215 (1)
	y	-0.0380 (9)	-0.0377 (8)	-0.0392 (7)	-0.0376 (8)
	z	0.784 (1)	0.784 (1)	0.784 (1)	0.783 (1)
	B	1.06 (5)	0.83 (4)	0.66 (4)	0.76 (4)
O 2B	x	-0.207 (1)	-0.207 (1)	-0.208 (1)	-0.205 (1)
	y	0.4656 (9)	0.4640 (7)	0.4655 (7)	0.4644 (8)
	z	-0.764 (1)	-0.763 (1)	-0.764 (1)	-0.778 (1)
	B	1.06 (5)	0.83 (3)	0.66 (4)	0.76 (4)
	R_p	7.0	5.9	6.4	5.7
	R_{wp}	9.2	7.6	8.2	7.5
	R_B	6.2	5.3	5.6	4.7
Mn1-O 1 2		1.928 (9)	1.947 (8)	1.942 (8)	1.95 (1)
Mn1-O 2A 2		2.013 (7)	2.026 (6)	2.035 (6)	2.022 (8)
Mn1-O 2A 2		1.994 (8)	1.986 (6)	1.981 (7)	1.971 (9)
Mn2-O 1 2		2.014 (9)	1.986 (8)	1.993 (8)	1.98 (1)
Mn2-O 2B 2		2.102 (7)	2.111 (6)	2.099 (6)	2.082 (8)
Mn2-O 2B 2		1.884 (8)	1.881 (6)	1.887 (6)	1.911 (9)
					1.891 (7)

diagram of the $\text{La}_1 \times \text{Ca}_x \text{MnO}_3$ compound depicted in Fig. 1 displays two distinct regions as the ground state is concerned. In the first region a canted antiferromagnetic (CAF) orthorhombic structure is present. In the second one, depending on x , a ferromagnetic insulating (FM I) monoclinic and orthorhombic structures have been observed. The change from CAF to FM I ground states occurs in a narrow concentration regime $0.12 < x / 0.14$, where in neutron diffraction patterns (vide infra) a ferromagnetic transition (T_c) is observed firstly and after an antiferromagnetic transition (T_N) have been observed upon cooling. Our high resolution synchrotron x-ray diffraction patterns revealed that the true symmetry of the samples in the boundary of the CAF and FM I regimes and partially in the FM I regime is monoclinic with very small monoclinic angle ($\gamma = 0.04 - 0.1^\circ$). This regime is denoted by symbol M^+ in the phase diagram. The temperature variation of the unit cell parameters in the FM I regime revealed an additional structural transformation which occurs upon heating from $T = 0$ at temperature

$T_{M^+ \rightarrow M^-}$. The magnitude of the unit cell changes at the $T_{M^+ \rightarrow M^-}$ reduces when the x is in the $\text{CAF} \rightarrow \text{FM I}(\text{M}^+)$ and $\text{FM I}(\text{M}^+) \rightarrow \text{FM I}(\text{O}^-)$ phase boundaries. In this phase diagram the ferromagnetic to paramagnetic (T_c), JT (T_{JT}) and $T_{M^+ \rightarrow M^-}$ transition lines are all estimated from neutron and magnetic measurements.

Figures 2, 3 and 4 (upper panels) show the temperature variation of the unit cell parameters for $x = 0.13; 0.15$ and 0.175 samples using the pseudo orthorhombic description of the unit cell. For $T < T_{JT}$, the unit cell parameters follow the inequality $a > c > b = 2$, a fact implying that in this pseudo orthorhombic description the O^- structure is realized in the whole temperature regime studied in this work. For all the samples there is a temperature region where the unit cell parameters change abruptly (a increases, $b = 2$ decreases and c decreases slightly) resembling the situation observed¹⁷ in the LaMnO_3 compound due to the orbital ordering state. As it is mentioned above, we define the transition temperature T_{JT} as the point where an extreme in the da/dT curve oc-

TABLE II: $\text{La}_1 \times \text{Ca}_x \text{MnO}_3$ ($x = 0.15$) structural parameters at several temperatures, as determined from Rietveld refinements based on neutron powder diffraction data of E9 diacetate ($\lambda = 1.79784 \text{ \AA}$). At $T = 320 \text{ K}$ the space group $\text{Pnm}\alpha$ (No 62) was used. La, Ca and apical oxygen (O1) occupy the $4c$, ($x;1=4;z$) site, Mn the $4b$ ($0;0;1=2$) site and the plane oxygen (O2) the general 8d site. For other temperatures the monoclinic space group $\text{P}2_1=c \text{ P}112_1=a$ (no 14, unique c-axis) was used. In this space group La, Ca O1, O2A and O2B occupy the general 4e position ($x;yz$). Mn1 and Mn2 occupy the 2c ($1/2,0,0$) and 2d ($1/2,1/2,0$) positions respectively. Numbers in parentheses are statistical errors of the last significant digit.

T (K)		320	250	170	100	2
a (Å)		5.5246 (1)	5.5573 (1)	5.5614 (1)	5.5480 (1)	5.5300
b (Å)		7.7877 (1)	7.7387 (1)	7.7266 (1)	7.7386 (1)	7.7508
c (Å)		5.5219 (1)	5.5213 (1)	5.5195 (1)	5.5159 (1)	5.5081
(deg.)		90	90.140 (1)	90.134 (2)	90.0965 (1)	90.0752
La, Ca	x	0.0263 (4)	0.0300 (3)	0.0311 (3)	0.0309 (3)	0.0303 (2)
	y	0.25	0.2489 (5)	0.2501 (7)	0.2493 (6)	0.2454 (6)
	z	-0.0083 (5)	0.0060 (4)	0.0060 (4)	0.0058 (4)	-0.0065 (4)
	B	0.54 (5)	0.40 (3)	0.42 (3)	0.12 (2)	0.15 (3)
Mn1	B	0.36 (7)	0.25 (5)	0.19 (5)	0.19 (5)	0.16 (5)
Mn2	B		0.25 (5)	0.19 (5)	0.19 (5)	0.16 (5)
O1	x	0.4910 (8)	0.4912 (4)	0.4914 (4)	0.4905 (5)	0.4909 (4)
	y	0.25	0.2450 (8)	0.246 (1)	0.2429 (8)	0.259 (1)
	z	0.0684 (7)	-0.0668 (4)	-0.0675 (1)	-0.0693 (4)	-0.0680 (5)
	B	0.94 (7)	0.69 (4)	0.58 (4)	0.45 (4)	0.484 (4)
O2A	x	0.2817 (6)	0.2180 (7)	0.2188 (8)	0.2212 (9)	0.2219 (9)
	y	0.0353 (3)	-0.0381 (5)	-0.0364 (7)	-0.0375 (6)	-0.0384 (6)
	z	0.7238 (6)	0.721 (1)	0.780 (1)	0.780 (1)	0.782 (1)
	B	0.88 (5)	0.63 (3)	0.58 (3)	0.40 (3)	0.32 (3)
O2B	x		-0.2075 (8)	-0.2059 (9)	-0.206 (1)	-0.2085 (0)
	y		0.4659 (6)	0.4639 (7)	0.4657 (7)	0.4666 (6)
	z		-0.766 (1)	-0.768 (1)	-0.768 (1)	-0.768 (1)
	B		0.63 (3)	0.58 (3)	0.40 (3)	0.32 (3)
	R_p	6.9	5.1	6.2	6.0	6.1
	R_{wp}	9.0	6.8	7.9	8.0	7.9
	R_B	4.3	4.1	5.6	3.7	3.6
Mn1-O1 2		1.9839 (8)	1.932 (6)	1.941 (8)	1.919 (6)	1.973 (7)
Mn1-O2A 2		2.006 (3)	1.999 (5)	1.996 (6)	1.986 (6)	1.973 (6)
Mn1-O2A 2		1.9634 (3)	1.992 (5)	1.991 (6)	1.995 (7)	2.002 (7)
Mn2-O1 2			2.007 (6)	1.994 (8)	2.026 (6)	1.975 (7)
Mn2-O2B 2			2.092 (5)	2.094 (6)	2.086 (6)	2.071 (6)
Mn2-O2B 2			1.886 (2)	1.893 (6)	1.891 (7)	1.893 (6)

cur, in the high temperature regime of the data. This particular assignment agrees with the magnetic measurements (vide infra). The orthorhombic strain parameters $\epsilon = 2(a - c)/(a + c)$ (see Figs. 2, 3 and 4, lower panels) becomes maximum at the ferromagnetic transition temperature. Furthermore, for $T < T_c$ ϵ decreases during cooling and finally for $T < T_{M=M} = 60 \text{ K}$ (for the $x = 0.13$ sample) it becomes almost temperature independent. The particular behavior reveals that the FM I state does not concern only the spin degrees of freedom but is also related with the lattice and orbital ones. The temperature variation of the unit cell volume $V(T)$ exhibits a discontinuous change at T_{JT} implying that the JT distortion is first order. As x increases the volume jump is difficult to be identified, on the basis of the available diacetate resolution. It is very likely that the JT structural transition becomes second order for $x = 0.175$. Above and below T_{JT} the unit cell volume decreases with temperature nearly linearly, showing a small slope change

at T_c . Finally, at $T_{M=M} = V(T)$ displays a pronounced slope change for all samples.

Let us present now the high resolution synchrotron x-ray data. The samples for 0.125×0.175 for $T < T_{JT}$ exhibited additional reflections that can not be accounted for the $\text{Pnm}\alpha$ space group. More specifically, we observed splitting of the $(hk0)$, and (hkl) diffraction peaks not allowed in the $\text{Pnm}\alpha$ space group. This splitting is compatible with the $\text{P}112_1=a \text{ P}2_1=c$ (no 14, unique c-axis) space group. Fig. 5 depicts the high resolution synchrotron x-ray diffraction data for the $\text{La}_{0.85}\text{Ca}_{0.15}\text{MnO}_3$ sample at $T = 5 \text{ K}$, as an example. One can see very clearly the splitting of the diffraction peaks with non zero h and k . We obtained similar data also for the other samples $x = 0.125 \times 0.175$. In this monoclinic distortion a glide-plane element is preserved, while the n and m elements are lost. The loss of the mirror plane may be signaling a change of the JT order from C type orbital ordering (that is followed by LaMnO_3) to a new one.

TABLE III: $\text{La}_{1-x}\text{Ca}_x\text{MnO}_3$ ($x = 0.175$) structural parameters at several temperatures, as determined from Rietveld refinements based on neutron powder diffraction data of E9 diatomite ($a = 1.79784 \text{ \AA}$). At $T = 300 \text{ K}$ the space group Pnmn (No 62) was used. La, Ca and apical oxygen (O 1) occupy the $4c$, ($x; z=1/4$) site, Mn in the $4b$ ($0; 0; z=1/2$) site and the plane oxygen (O 2) the general $8d$ site. For other temperatures the monoclinic space group $\text{P}2_1=c \text{ P}1 \text{ 1} \text{ 2}_1=a$ (No 14, unique c -axis) was used. In this space group La, Ca O 1, O 2A and O 2B occupy the general $4e$ position ($x; y; z$). Mn 1 and Mn 2 occupy the $2c$ ($1/2, 0, 0$) and $2d$ ($1/2, 1/2, 0$) positions respectively. Numbers in parentheses are statistical errors of the last significant digit.

T (K)		300	200	170	120	70	2
a (Å)		5.5113 (1)	5.5275 (1)	5.5323 (1)	5.5242 (1)	5.5165 (1)	5.5152 (1)
b (Å)		7.7778 (1)	7.7449 (2)	7.7414 (1)	7.7453 (1)	7.7553 (1)	7.7568 (1)
c (Å)		5.5142 (1)	5.5114 (1)	5.5104 (1)	5.5080 (1)	5.5050 (1)	5.5042 (1)
(deg.)	90.0		90.094 (6)	90.09 (1)	90.063 (5)	90.059 (4)	90.056 (4)
La, Ca	x	0.0252 (4)	0.0283 (3)	0.0292 (5)	0.0290 (3)	0.0280 (3)	0.0278 (3)
	y	0.25	0.248 (1)	0.244 (1)	0.247 (1)	0.249 (1)	0.248 (1)
	z	-0.008 (1)	0.0063 (5)	0.0087 (7)	0.0074 (5)	0.0070 (6)	0.0077 (6)
	B	0.57 (4)	0.44 (3)	0.70 (4)	0.37 (3)	0.28 (3)	0.28 (3)
Mn 1	B	0.37 (7)	0.1 (1)	0.34 (8)	0.08 (6)	0.11 (6)	0.13 (6)
Mn 2	B		0.1 (1)	0.34 (8)	0.08 (6)	0.11 (6)	0.13 (65)
O 1	x	0.4927 (8)	0.4914 (6)	0.4910 (8)	0.4927 (6)	0.4913 (6)	0.4913 (5)
	y	0.25	0.247 (1)	0.246 (1)	0.248 (1)	0.250 (1)	0.251 (1)
	z	0.0680 (8)	-0.0669 (5)	-0.0646 (7)	-0.0671 (5)	-0.0665 (6)	-0.0673 (3)
	B	0.86 (7)	0.65 (5)	0.77 (6)	0.46 (5)	0.38 (5)	0.37 (5)
O 2A	x	0.2792 (7)	0.221 (1)	0.221 (2)	0.224 (1)	0.221 (1)	0.221 (1)
	y	0.0344 (4)	-0.035 (1)	-0.0360 (9)	-0.0369 (8)	-0.033 (1)	-0.033 (1)
	z	0.7240 (7)	0.781 (1)	0.771 (2)	0.770 (1)	0.781 (1)	0.778 (2)
	B	0.7224 (7)	0.62 (3)	1.04 (5)	0.64 (4)	0.50 (3)	0.56 (4)
O 2A	x		-0.209 (1)	-0.209 (2)	-0.208 (1)	-0.213 (1)	-0.214 (1)
	y		0.464 (1)	0.4676 (9)	0.4666 (9)	0.462 (1)	0.462 (1)
	z		-0.766 (1)	-0.771 (2)	-0.780 (1)	-0.770 (1)	-0.774 (2)
	B		0.62 (4)	1.04 (5)	0.64 (4)	0.50 (3)	0.56 (4)
	R_p	6.0	5.4	6.8	5.8	6.1	6.2
	R_{wp}	8.0	7.0	9.4	7.6	8.0	8.0
	R_B	3.3	3.6	5.6	4.2	3.8	3.8
Mn 1-O 1 2		1.9809 (1)	1.949 (1)	1.93 (1)	1.95 (1)	1.979 (1)	1.98 (1)
Mn 1-O 2A 2		1.996 (4)	1.973 (8)	2.00 (1)	2.000 (8)	1.968 (8)	1.980 (9)
Mn 1-O 2A 2		1.973 (4)	1.995 (8)	1.95 (1)	1.959 (8)	1.989 (9)	1.97 (1)
Mn 2-O 1 2			1.993 (1)	1.99 (1)	1.98 (1)	1.96 (1)	1.96 (1)
Mn 2-O 2B 2			2.074 (8)	2.04 (1)	2.029 (8)	2.043 (8)	2.028 (9)
Mn 3-O 2B 2			1.891 (8)	1.92 (1)	1.944 (9)	1.922 (8)	1.93 (1)

We note that similar monoclinic distortion have been detected in $\text{La}_{1-x}\text{Sr}_x\text{MnO}_3$ ($x = 0.11-0.5$) compounds.¹⁸ Based on this critical information about the symmetry of the structure we refine the neutron data using the $\text{P}2_1=c$ space group. The mirror plane at $y = 1/4$ being present for Pnmn space group is now absent, resulting in two Mn sites along the b axis, the first at $(1/2, 0, 0)$ and the second at $(1/2, 1/2, 0)$. Similarly, instead of one plane oxygen site (O 2, Pnmn symmetry) there are two now in the $\text{P}2_1=c$ symmetry. Thus, in this new symmetry two crystallographically independent Mn sites produce a layer type arrangement of two different MnO₆ octahedra along the b axis. The refinement strategy employed in this work was to first optimize the scale factor, background, unit cell parameters and zero-shift errors. Subsequently, we refined the atomic positional and isotropic thermal parameters. In order to reduce the number of parameters we decided to refine the thermal parameters for all the sites isotropically and we kept equal the ther-

mal parameters of the Mn and O 2 sites. Figures 6 and 7 show two representative Rietveld plots of neutron data for $\text{La}_{0.85}\text{Ca}_{0.15}\text{MnO}_3$ sample at 320 K and 2 K, respectively. The corresponding structural parameters for all the studied samples are reported in Tables I-III.

Fig. 8 shows projections of the monoclinic structure of the $\text{La}_{0.85}\text{Ca}_{0.15}\text{MnO}_3$ compound for $T = 170 \text{ K}$ on the bc and ab planes, respectively. All the samples show qualitatively the same behavior, as far as the variation of the structural parameters with temperature is concerned. Nevertheless, there are significant quantitative differences related to the influence of the hole doping through Ca substitution.

The Bragg peaks are quite sharp for $T > T_c$ (x) but for $T < T_{JT}$ they develop a pronounced selective peak broadening. In order to account for the selective peak broadening the Stephens¹⁹ microstrain model was used. As our Rietveld refinement results reveal the microstrain parameters follow the temperature variation of the unit cell

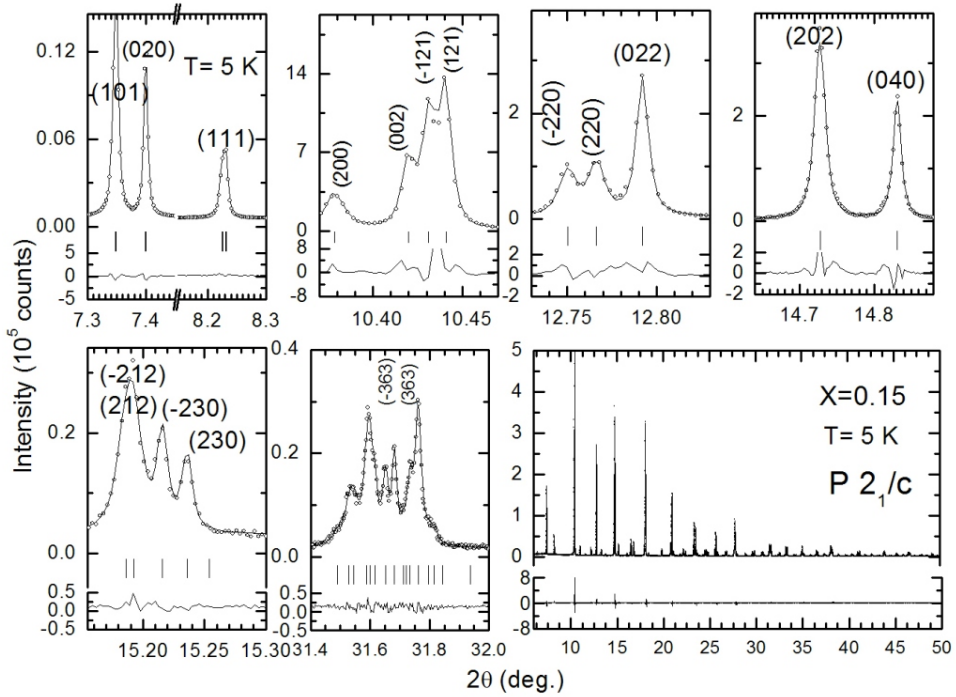


FIG. 5: Rietveld plot for $\text{La}_{0.85}\text{Ca}_{0.15}\text{MnO}_3$ at $T = 5 \text{ K}$ using the high resolution x-ray diffraction data from ID 31 beam line of the ESRF. Shows details of the diffraction peaks where the characteristic peak splitting compatible with $\text{P } 2_1/\text{c}$ space group is expected.

parameters. The most significant broadening is related to S_{202} and S_{400} parameters. The S_{202} strain parameter describes a correlated type random strain between a and c crystallographic directions and it is reasonable to be attributed to some kind of local static orbital ordering correlations. The average structure revealed a cooperative JT distortion which increases as temperature decreases. Parallel to this behavior, there is an antagonistic interaction which produces correlated fluctuation of the cell constants. These fluctuations are directly connected with the development of the ferromagnetic long range order and temperature variation of the unit cell parameters. The microstrain parameters take the maximum value at T_c . Most importantly the microstrain parameters are reduced about 30% at $T_{\text{Mn}} = 100 \text{ K}$ and below this temperature remain nearly temperature independent. Consequently, our structural data reveal a complex magneto-elastic behavior for $T < T_c$, that characterizes the FM I regime of the $\text{La}_{1-x}\text{Ca}_x\text{MnO}_3$ compound.

Anisotropic broadening is usually connected with the presence of correlated structural defects, due to the preparation method, or is inherent to structural magnetic transformations. Since we observe temperature dependence in the microstrain parameters, the case of the structural defects caused by the preparation method should be ruled out, because in this case a temperature independent behavior is expected. It is natural to ask what is the physical origin of the particular temperature variation of the microstrain parameters. Essentially, the

anisotropic peak broadening concerns the lattice planes $(h00)$ and $(h01)$, meaning that there is some modulation along the a -axis and $a + c$ -direction. Our findings may be related with recent theoretical studies where the important role of the elastic energies (strain) in determining the ground state of the system has been pointed out.^{20,21} Furthermore, the anisotropic broadening may originate from grains which contain different structural domains corroborated by the successive magneto-structural transformation occurring upon cooling. Finally, one cannot disregard the case where phase separation is present especially near the CAF-FM I phase boundary. In such a case several phases with nearly similar parameters occur producing indirectly a selective peak broadening, which is accounted for by microstrain formalism.

IV. BOND LENGTHS

In Fig. 9 are depicted the temperature variation of the Mn-O bond lengths for $x = 0.125, 0.15$ and 0.175 samples, deduced from neutron diffraction data. For $T < T_{\text{JT}}$ the crystal structure of the $\text{La}_{1-x}\text{Ca}_x\text{MnO}_3$ in the FM I regime based on the $\text{P } 2_1/\text{c}$ space group have two Mn sites. As the Ca content increases the long Mn2-O bond length (which has been attributed to the d_{z^2} orbital) decreases. The short Mn2-O bonds are approximately at the same level as in the LaMnO_3 case. Concerning the intermediate Mn2-O bond, its magnitude is above

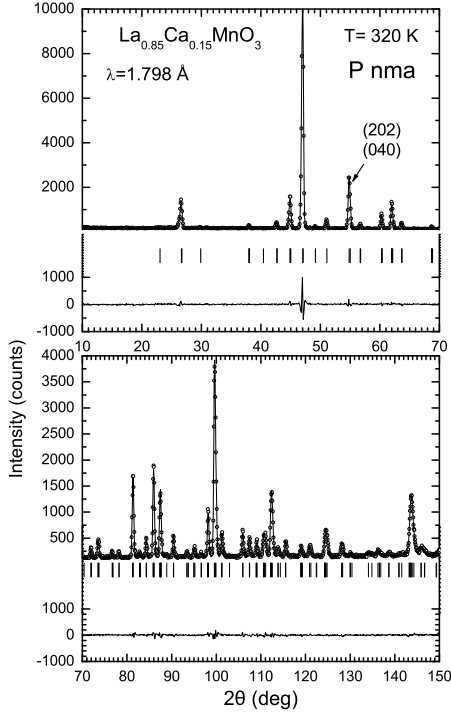


FIG. 6: Rietveld plot for $\text{La}_{0.85}\text{Ca}_{0.15}\text{MnO}_3$ at $T = 320\text{ K}$. The observed data points are indicated by open circles, while the calculated and difference patterns are shown by solid lines. The positions of the reflections are indicated by vertical lines below the patterns.

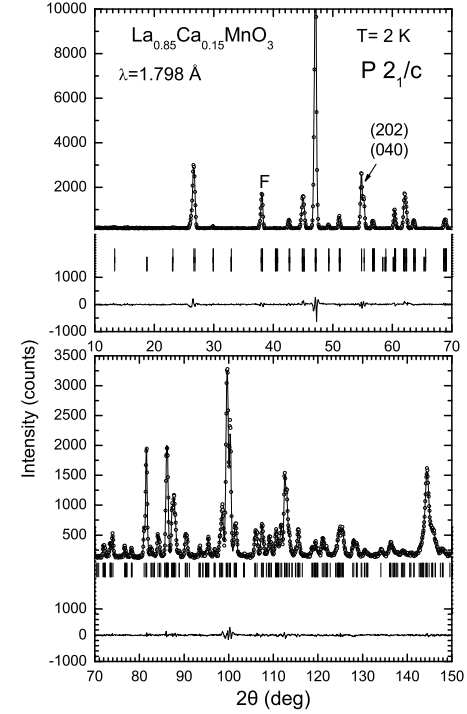


FIG. 7: Rietveld plot for $\text{La}_{0.85}\text{Ca}_{0.15}\text{MnO}_3$ at $T = 2\text{ K}$. The observed data points are indicated by open circles, while the calculated and difference patterns are shown by solid lines. The positions of the reflections are indicated by vertical lines below the patterns.

the corresponding one of LaMnO_3 . It is interesting to note that the long and short bonds follow the temperature variation of the a and c cell parameters or in other words these bonds define the temperature variation of the unit cell parameters. Based on the similarities of the Mn_2O bond lengths with those of LaMnO_3 , it is reasonable to attribute the Mn_2 site to a Mn^{+3} like site in the $\text{La}_{1-x}\text{Ca}_x\text{MnO}_3$ ($0.125 \leq x \leq 0.175$) compound.

Let us turn now to the $\text{Mn}_1\text{-O}$ bond lengths. As their magnitude is concerned these bond lengths, are more close to the bond lengths of MnO_6 , observed in the FM M region of the phase diagram. In Fig. 9 (upper panel) with bold lines, the $\text{Mn}_1\text{-O}$ bond lengths observed in $\text{La}_{0.75}\text{Ca}_{0.25}\text{MnO}_3$ compound are depicted. One can see that as x increases the $\text{Mn}_1\text{-O}$ bond lengths approach these lines. It is plausible to attribute the Mn_1 site to a mixed valence Mn like site as observed in the $\text{La}_{0.75}\text{Ca}_{0.25}\text{MnO}_3$ compound. As x reduces towards the CAF regime the $\text{Mn}_1\text{-O}$ bond lengths become non-degenerated and move away from those of $\text{La}_{0.75}\text{Ca}_{0.25}\text{MnO}_3$ compound.²²

Except for the geometrical variation of the bond lengths there is an orientation difference, concerning the short $\text{Mn}_1\text{-O}$ bonds ($i = 1, 2$), between the two Mn -sites. In the Mn_2 -site (which resembles the LaMnO_3 case) the short

bond lies in the ac plane, contrary to the Mn_1 -site, where the short $\text{Mn}_1\text{-O}$ bond is directed, approximately, along the b -axis. According to the authors' opinion this is the key point to which one can be based in order to explain the FM I phase. It is important to note the fundamental difference between the conventional JT orthorhombic O^+ and the monoclinic M^+ structures. The latter cannot be the usual C-type antiferrodistortive arrangement found in the O^+ structure in LaMnO_3 and CAF part of the phase diagram. As proposed by Cox et al.¹⁸ in the case of $\text{La}_{1-x}\text{Sr}_x\text{MnO}_3$, the loss of the mirror plane would be consistent with a change in JT order from C-type to G-type at which there is antiferrodistortive coupling of MnO_6 octahedra along the b direction instead of parallel coupling (see Fig. 8).

V. MAGNETIC MEASUREMENTS AND MAGNETIC STRUCTURE

Fig. 10 and Fig. 11 (upper panels) show the temperature variation of the magnetic moment per Mn ion for the samples $x = 0.15$ and 0.175 , respectively, for several dc magnetic fields. We obtained similar magnetic measurements data also for $x = 0.125; 0.13$ and 0.14 samples.

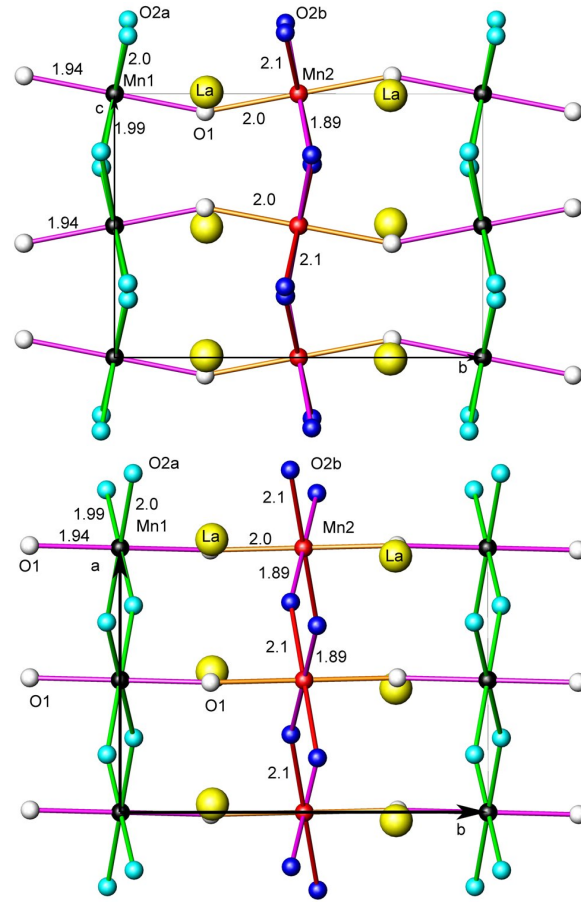


FIG. 8: Crystal structure of $\text{La}_{0.85}\text{Ca}_{0.15}\text{MnO}_3$ compound at $T = 170$ K. The upper and lower panels show the projections along the a and c axis, respectively. The large hatched, small filled and intermediate open spheres represent La, Mn and O ions respectively. The Mn1, Mn2 sites are located at $y = 0$ and $y = 1/2$ planes respectively (b axis is the largest one). The short Mn1-O, Mn2-O bonds denoted by grey rods are directed along and perpendicular to the b -axis, respectively.

In the lower panels of Figs. 10, and 11 we plot the temperature dependence of the normalized real part of the ac susceptibility, and the low field dc magnetic moment (left axis). In addition, we plot the temperature variation of the inverse dc susceptibility ($H = m$) (right axis) measured under a dc field $H = 5$ kOe. The abrupt increasing of the magnetic signal in the dc and ac measurements at $T_c = 168$ K and $T_c = 187$ K for $x = 0.15$ and $x = 0.175$ respectively marks a transition from a paramagnetic to ferromagnetic state, in agreement with neutron data (vide infra). The sharp peak at T_c in the χ^0 is related with the Hopkinson effect, as we discussed in Ref. 9. Upon heating from $T = 0$, $\chi^0(T)$ slightly increases up to $T = T_{\text{M}=\text{M}^{\text{--}}}$. For $T > T_{\text{M}=\text{M}^{\text{--}}}$, $\chi^0(T)$ increases in a step wise fashion as the dashed vertical lines in Figs. 10 and 11 show. This peculiarity reveals the magnetic signature of the structural change that occurs at $T_{\text{M}=\text{M}^{\text{--}}}$. The particular anomaly is present and in the

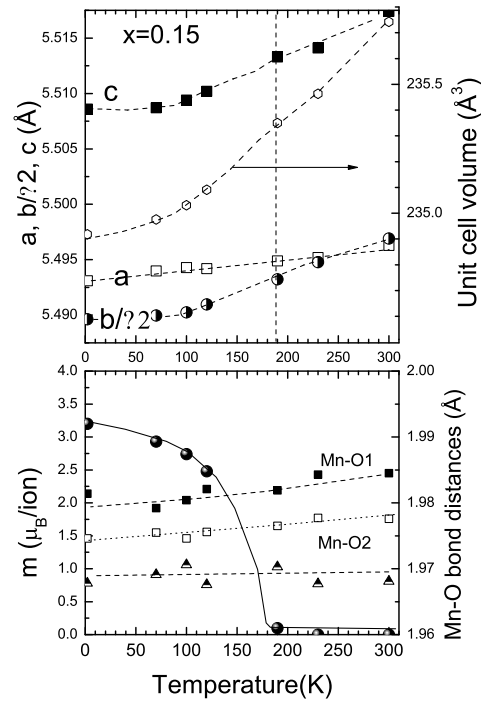


FIG. 9: $\text{Mn}-\text{O}_i$ ($i = 1, 2$) bond distances as a function of temperature for $x = 0.125, 0.15$ and 0.175 samples. The upper panel shows the $\text{Mn}1-\text{O}$ bonds and lower panel the $\text{Mn}2-\text{O}$ bonds ($\text{Mn}1-\text{O}_1, \text{Mn}2-\text{O}_1$ are the apical bonds and $\text{Mn}1-\text{O}_2\text{A}, \text{Mn}2-\text{O}_2\text{B}$ are the in-plane bonds). Lines through the experimental points are guides to the eye. The solid, open and "crossed" symbols correspond to $x = 0.125, 0.15$ and 0.175 respectively. The data for the LaMnO_3 (thin lines) and $\text{La}_{0.75}\text{Ca}_{0.25}\text{MnO}_3$ (thick lines) samples are also included for a direct comparison.

dc magnetization measurements as it is seen for example, in the upper panel of the Fig. 10 where a step like slope change occurs at $T_{\text{M}=\text{M}^{\text{--}}}$.

Furthermore, a close inspection of the $m(T)$ curves at the paramagnetic regime reveals an additional anomaly which is related with JT distortion observed in the crystal structure data (see inset of Fig. 10). This anomaly is more pronounced for $x = 0.11$ sample, its signature reduces as x increases and finally becomes hard to discern for the samples with $x = 0.175$. The anomaly in the magnetic measurements at T_{JT} is seen more clearly in the inverse susceptibility data (see lower panels of Fig. 10 and Fig. 11). Comparing these data one can clearly see that the jump of $H = m$ at T_{JT} is transformed to a slope change as x increases. The particular change at T_{JT} for the $x > 0.175$ samples may mark a change of JT transition from first to second order.

Above and below T_{JT} , χ^1 can be fitted by a straight line implying a Curie-Weiss law ($\chi^1 = (T - \theta) = C$). The Curie constant is given by $C = (N = V_c)g^2 \mu_B^2 S(S+1) = 3k_B$, where N is the number of magnetic ions inside the unit

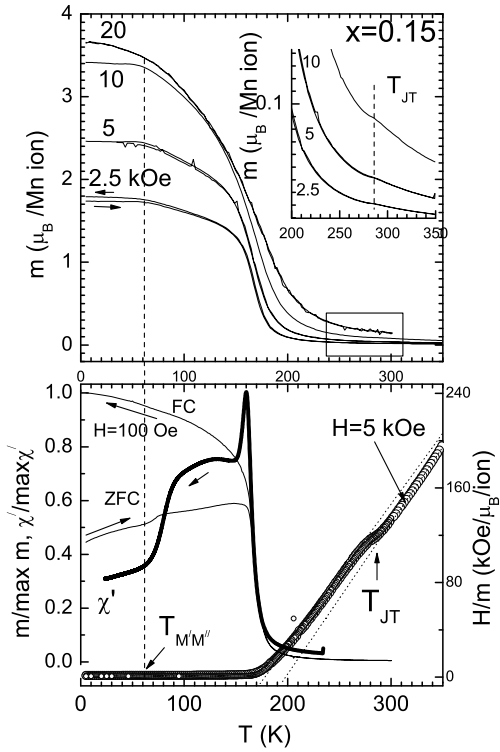


FIG . 10: (upper panel) Temperature variation of the bulk magnetic moment per ion Mn for $\text{La}_{0.85}\text{Ca}_{0.15}\text{MnO}_3$. The data were collected under the indicated magnetic fields using the standard ZFC-FC procedure. The inset shows the details of the measurements at the T_{JT} region. (lower panel) Temperature variation of the inverse dc magnetic moment, normalized real part of the fundamental ac-susceptibility (bold line) and normalized ZFC and FC bulk magnetic moment measured under a dc field 100 Oe (thin line). The dot lines corresponds to the Curie-Weiss law used to fit the data above and below T_{JT} . The vertical dashed line indicates the $T_{JT} = 175 \text{ K}$.

cell, V_c is the unit cell volume, g is the Lande factor, μ_B is Bohr magneton, S the spin of the ion, k_B is Boltzmann's constant and χ is the Weiss constant. Since \mathbf{m}^1 is nearly parallel above and below T_{JT} it is reasonable to attribute this change to magnetic clusters.^{23,24} The larger effective magnetic moment of the M^+ phase for $x > 0.15$ may be related with the idea of magnetic polaron that "survives" in the regime $T_c < T < T_{JT}$. We must note that this state is more relevant when the system moves away from the CAF regime. Finally, it is interesting to note the similarity of our bulk magnetic moment data with those of Refs. 23,24 referring to the Sr-compound. There is however a distinct difference below T_c . Our ac susceptibility, reduces significantly for $T < T_{M^+M^{++}}$, while in the Sr-case it increases in a stepwise fashion. This "new" difference may imply that the M^{++} states of Ca and Sr compounds are different. The orthorhombic strain and the long in-plane Mn-O₂ distance reduction is very similar but the ordered magnetic moment, bulk magnetic moment and ac susceptibility show opposite change at $T_{M^+M^{++}}$.

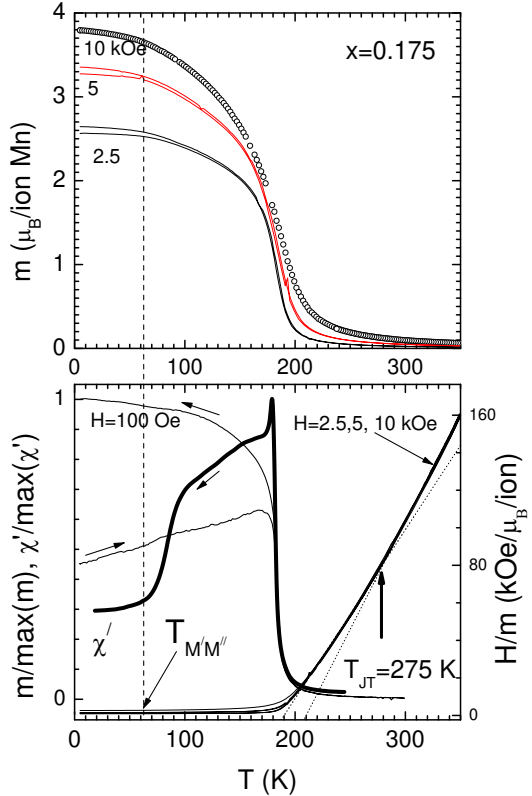


FIG . 11: (upper panel) Temperature variation of the bulk magnetic moment per ion Mn for $\text{La}_{0.825}\text{Ca}_{0.175}\text{MnO}_3$. The data were collected under the indicated magnetic fields using the standard ZFC-FC procedure. (lower panel) Temperature variation of $H=m$, normalized real part of the fundamental ac-susceptibility (bold line) and normalized ZFC and FC bulk magnetic moment measured under a dc magnetic field 100 Oe (thin line). The dot lines corresponds to the Curie-Weiss law used to fit the data above and below T_{JT} . The vertical dashed line indicates the $T_{M^+M^{++}} = 275 \text{ K}$.

Let us present now the neutron diffraction data related with the magnetic structure. The magnetic structures for all the samples are best monitored by observing the neutron diffraction patterns, using data from E6 instrument

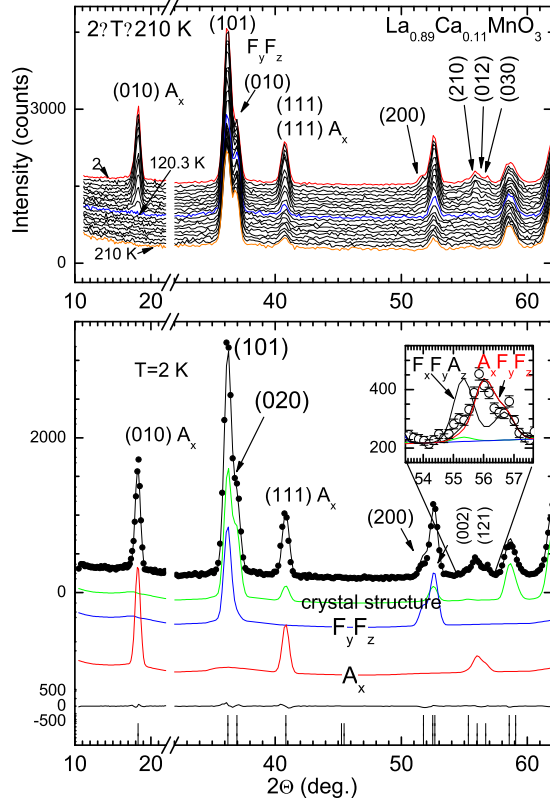


FIG. 12: (Upper panel) Selected portion of the neutron powder diffraction patterns for $\text{La}_{0.89}\text{Ca}_{0.11}\text{MnO}_3$ for $T = 2\text{ K}$ and $T = 210\text{ K}$. (Lower panel) Decomposition of the neutron diffraction pattern as $T = 2\text{ K}$. Shown are the profiles coming from the A-antiferromagnetic, the ferromagnetic and crystal structures. The inset shows the observed and calculated profiles for the Bragg peaks (210) , (012) and (030) based on the models $F_x F_y A_z$ and $A_x F_y F_z$.

with $\gamma = 2.4\text{A}$. Fig. 12 show portions of neutron diffraction patterns in the region where the magnetic coherent intensity is maximum for $x = 0.11$ sample. Similar data were also collected for the other samples. In all samples we observed an increasing of the Bragg intensity for the peaks (101) and (020) for $T < T_c$, something which is compatible with the development of long range ferromagnetic order. In addition, the samples $x = 0.11, 0.125$ and 0.13 show the characteristic magnetic peaks of the A-antiferromagnetic structure. The most pronounced magnetic Bragg peak of the A-magnetic structure is the (010) located at 18° . As x increases, the area of this peak at $T = 2\text{ K}$ reduces, implying that the antiferromagnetic ordered moment reduced and finally becomes zero for $x = 0.14$. We refined the $x = 0.11$ sample, where the pronounced orthorhombicity enables us to safely determine the spin components along the three axes. The lower panel of Fig. 12 shows a decomposition of the neutron diffraction pattern at $T = 2\text{ K}$, which consists of the

patterns coming from the A-type antiferromagnetic, the ferromagnetic and the crystal structure patterns. The inset of the lower panel of Fig. 12 shows the calculated patterns of models $F_x F_y A_z$ and $A_x F_y F_z$ (F_x denotes ferromagnetic moment along x-axis and A_x magnetic moment along x-axis which follows the A-antiferromagnetic structure). The agreement between the theoretical and experimental profile is better for the $A_x F_y F_z$ model. This magnetic model is closely connected with the canted magnetic structure observed in the LaMnO_3 compound.²⁵ Similarly, for $x = 0.125$ sample, except for the major ferromagnetic component, small intensity coming from A-type antiferromagnetic structure is present. In addition, the negligible intensity of the (200) magnetic peak, implies that the ferromagnetic component cannot be parallel with b-axis. Therefore there are two possibilities. The first is the antiferromagnetic component to be parallel with the c-axis, while the ferromagnetic component parallel with a and b axis. The second possibility is both the antiferromagnetic and part of the ferromagnetic component to be parallel with a-axis. Since it is not possible to have simultaneous ferromagnetic and antiferromagnetic spin components along the a-axis in the same domain these two different magnetic states concern different domains. This finding is not strange since in this concentration regime the phase boundary separating the CAF and FM I ground states exists.

For the sample $x = 0.15$ the NPD at $T = 2\text{ K}$ shows only ferromagnetic magnetic peaks. The orthorhombicity of the sample permits the calculation of the orientation of the magnetic moment in respect of the crystallographic axes. Thus, the case m jy-axis should be excluded. If the magnetic moment was along the b-axis the magnetic contribution at the (020) peak should be zero. Based on the best agreement between observed and theoretically calculated profiles we conclude that the ordered magnetic moment should be lie on the ac-plane with its larger component along the a-axis. Nevertheless, a small component along the b-axis cannot be totally excluded. The ordered magnetic moments as estimated from Rietveld refinements for the $x = 0.13, 0.15$ and 0.175 samples are plotted in the lower panels of Figs. 2, 3 and 4, respectively. A weak but distinctive anomaly is present in the temperature variation curves of the ordered magnetic moments at $T_{M-M} = 0$. It is imperative to note that for $T = T_{M-M} = 0$ the ordered magnetic moment curve, for $x = 0.15$ and 0.175 samples, displays a small slope change. For samples $x = 0.11, 0.125$ and 0.13 where we can detect the magnetic peak from the A-type magnetic structure, this anomalous behavior certainly is related with the antiferromagnetic component. For $x = 0.15$ it is possible that a small percentage of the spin of Mn ions may prefer a glass-like behavior for $T < T_{M-M} = 0$, as the ac susceptibility measurements show.²⁶ Concerning this "strange" magnetic component it is not clear how it is connected with the structural transition at the same temperature. One could invoke the idea of the phase separation to explain this behavior, however, the bulk char-

acter of the concomitant structural transition at $T_{M=M} = 0$ is not so favorable for this interpretation. Based on the experimental data one may say that the structural transition prevents some part of the Mn-spin to participate in the long-range ordering.^{9,26} This structural transition should be related with the orbital degree of freedom in agreement with Mössbauer²⁷ and NMR²⁸ data.

V I. DISCUSSION

Unexpectedly, the space group $P\bar{2}_1=c$ has been used by Lobanov et al.,²⁹ in order to describe the crystal structure for a sample with nominal stoichiometry $La_{0.85}Ca_{0.15}MnO_3$ prepared by liquid road and ball-reaction temperature $900^\circ C$. However, although this space group is the same with that used in our study, several differences exist. More specifically: (a) The ac susceptibility and resistivity data are different. (b) The sample of Lobanov et al.,²⁹ does not show the pseudo-orthorhombic splitting seen in our data and in the $La_{1-x}Sr_xMnO_3$ compound. The lattice parameters follow a monotonic temperature variation, contrary to ours. (c) The particular arrangement of the short bonds of Mn1-O and Mn2-O is different with it deduced from our data. Since no more data, from samples prepared with method of Ref. 29, are available, we cannot safely further comment on the possible relation between the two studies.

It is interesting to discuss our crystal structure data in terms of the normal coordinates⁷ of the octahedral complex MnO₆, Q₃ and Q₂. An arbitrary e_g orbital state can be written as $j_i = \cos(\theta/2)j_{z^2}i + \sin(\theta/2)j_{x^2-y^2}i$. The orbitals $j_{z^2}i$ and $j_{x^2-y^2}i$ correspond to the states $j = 0i$ and $j = i$ respectively. It is also possible, the orbitals $(j_{x^2}i, j_{y^2}i)$ and $(j_{z^2}x^2i, j_{z^2}y^2i)$ to be formed. In this case we have $j = (2-3)i$ and $j = (1-3)i$, respectively. Experimentally the orbital filling can be estimated from crystallographic data, through the Mn-O bond lengths using the equation^{7,8} $\tan \theta = Q_2/Q_3$, where $Q_3 = 2 = 6(2m-1)s$ and $Q_2 = 2(1-s)$. Here l; m and s mean long, medium and short Mn-O bond lengths, respectively. Q₂ mode mixes the $j_{x^2-y^2}i$ and $j_{z^2}i$ orbitals and produces a two sublattice orbital ordering pattern, with a lower energy orbital $g = c_1j_{x^2-y^2}i - c_2j_{z^2}i$ and a higher energy orbital $e = c_2j_{x^2-y^2}i + c_1j_{z^2}i$ (i is referring to the two sublattices).

Using the crystallographic data at $T = 300 K$ of $LaMnO_3$ (Ref. 17) one finds, $Q_3 = 0.121\text{Å}$ and $Q_2 = 0.383\text{Å}$. These values correspond to a canted antiferromagnet like orbital arrangement with two sublattices, with $\theta = 72.38^\circ$, respectively. Based on the crystallographic data of the present study we calculated the Q₂ and Q₃ parameters for the two sites predicted from $P\bar{2}_1=c$ structural model. Fig. 13 shows the temperature variation of Q₂ and Q₃ for the $x = 0.125; 0.15$ and 0.175 samples. With solid lines we also plot the values which correspond to the $LaMnO_3$ compound. The first

comment which can be made is that both Q₂ and Q₃ parameters for the two sites have lower values, in comparison to these of the $LaMnO_3$ compound. The second one is that, both Mn sites have Q₃ = 0 with the first displaying a high value while the second a moderate one. Since we only have a small number of data it is difficult to recognize any change at $T_{M=M} = 0$. The third comment is that, only the sample $x = 0.125$ shows a non monotonic variation of Q₂ at $T_{M=M} = 0$. We note that for $T > T_{JT}$ the two sites pattern collapse into one site, with both Q₂ and Q₃ modes taking values near zero.

A. The comparison with Sr-compound

First of all, we must point out the similarities between the Sr and Ca based compounds, by comparing the neutron data from the stoichiometric $La_{1-x}Sr_xMnO_3$ ($0.1 \leq x \leq 0.2$) of Dabrowski et al.^{30,31} with ours. As Dabrowski et al. have pointed out,³⁰ the phase diagrams of the Sr case reported in the recent literature were constructed using physical and structural information obtained for similar samples. Specifically, in the doping regime $0 \leq x \leq 0.3$ of Sr-compound the structure can form vacancies on both the A (La,Sr) and B (Mn) sites during synthesis under oxidizing conditions. Formation of equal number of vacancies on the A and B sites would increase the average Mn oxidation state. Let us discuss our results with those of single crystal data of $La_{7-8}Sr_{1-8}MnO_3$ compound (this concentration is the most representative and widely studied of the particular regime) where very interesting results are available.

In a recent resonant x-ray scattering study on a $La_{7-8}Sr_{1-8}MnO_3$ single crystal, Gack et al.,³² have shown that the orbital state occurring in the interval $T_{MT} \leq T \leq T_{JT}$, (M means monoclinic and T triclinic) is similar to that found in $LaMnO_3$. For $T < T_{MT}$ an orbital reordering is compatible with the resonant data. This group³² observed non zero resonant and nonresonant intensity at $(3/2, 3/2, 3)$ superlattice reflection, only for $T < T_{MT}$. The nonresonant scattering in the particular reflection implies some kind of a superstructure modulation that develops at $T = T_{MT}$. Such behavior is related to structural and electronic degrees of freedom, speculatively attributed to the orbital polarons formation.^{33,34} The work of Gack et al.,³² further supports the aspect that the CaF and FM I phases of Ca and Sr based $La_{1-x}(Ca,Sr)_xMnO_3$ compounds have both common characteristics, and distinct differences. It seems that the vertical boundary of the Sr-case that separates the $O^=$ CaF ground state from the triclinic new unknown orbital state exists even in the Ca-case. Our results show that: (a) Similar to the Sr compound for $T_{MT} \leq T \leq T_{JT}$ the structure is monoclinic ($P\bar{2}_1=c$). (b) Based on our high resolution synchrotron x-ray diffraction data, the crystal structure of the Ca case remains monoclinic, while in the Sr case it is triclinic and (c) both families of compounds exhibit significantly lower JT dis-

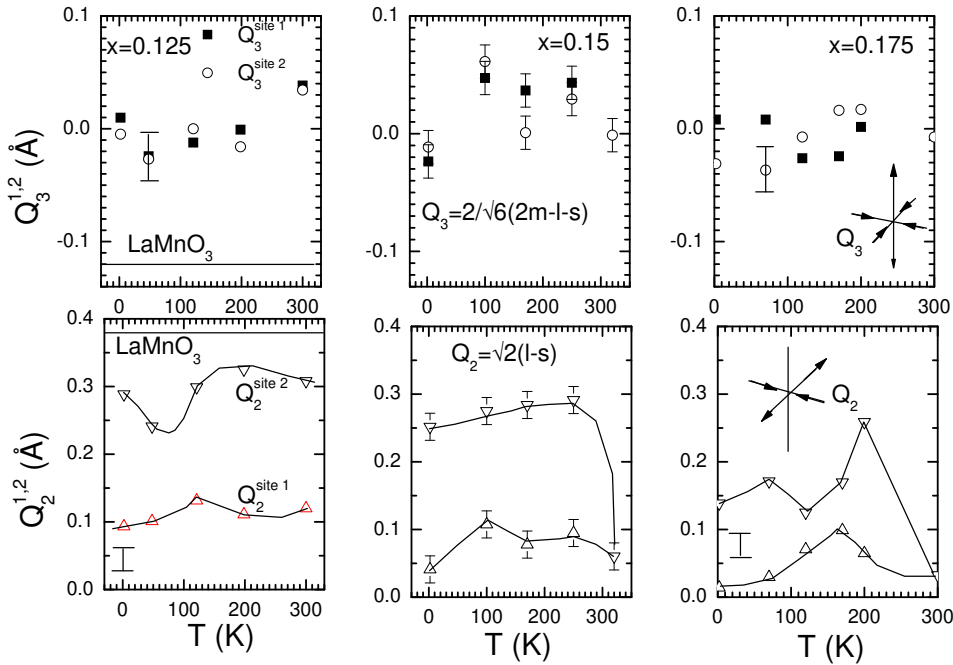


FIG. 13: Temperature variation of the Q_2 and Q_3 parameters for $\text{La}_{1-x}\text{Ca}_x\text{MnO}_3$ ($x = 0.125, 0.15$ and 0.175) samples. The data for the LaMnO_3 compound are also included for a direct comparison (thin line).

tortion in comparison with the M^+ phase which occurs for $T_{M^+M^+} < T < T_{JT}$.

B. Comparison between stoichiometric and cation deficient samples

We would like to emphasize once again that our results concern stoichiometric samples. The stoichiometric samples have properties different from those prepared in air.^{9,35,36} The most prominent differences between the two families of samples are that the oxygen deficient samples do not display the CAF structure and do not undergo the characteristic cooperative JT distortion, irrespectively of the nominal calcium concentration. The second difference makes the cation deficient samples to be in an orbital liquid state below T_c , in the FM I regime, contrary to the stoichiometric ones where the ferromagnetic phase takes place in the cooperative ordered JT state at least in the interval $T_{M^+M^+} < T < T_c$. In addition, the cation deficient samples (e.g. $x = 0.1, 0.15$ samples^{35,37}) show an almost monotonic variation with temperature of the unit cell parameters, satisfying also the inequality $c > a > b = \sqrt{2}$ (for $T < T_c$), contrary to the behavior observed in our stoichiometric samples where a pronounced non monotonic variation is observed. It is now well established that for low Ca concentrations the air prepared samples have cation vacancies.^{9,10,11} The amount of vacancies increases as the nominal Ca concentration is near $x = 0$. These samples are ferromagnetic irrespectively of x . The ordered magnetic moment at zero temperature

is significantly lower than the corresponding moment of the stoichiometric samples. For the $x = 0.1$ and 0.15 non stoichiometric samples the ordered magnetic moment was found $3\beta_B$ (Refs. 35,37,38), while in our stoichiometric samples are obtained $3.7\beta_B$.

In order to check once more the situation we selected the $x = 0.15$ sample, prepared in air for a detailed structural characterization using neutron diffraction data. Fig. 14 shows the temperature variation of the unit cell parameters (upper panel), the ordered magnetic moment and the Mn-O bond lengths (lower panel), as they were deduced from neutron diffraction data using E9 instrument. In perfect agreement with the above, this sample is ferromagnetic insulator without the orthorhombic splitting that characterizes the cooperative JT distortion of the reduced samples. Interestingly, the ordered magnetic moment is lower than the one of the reduced samples (e.g. 3.2 vs $3.7\beta_B$).

In the work of Igarabe et al.³⁸ that concerns a cation deficient sample with nominal $x = 0.1$, significant small angle neutron scattering intensity (due to nanometric clusters) has been found to coexist with the long-range ferromagnetic phase. In our opinion, it is difficult to correlate this nanometric clusters with the anomalies observed for $T < T_{M^+M^+}$ in the stoichiometric samples because these clusters may be related with cation vacancies. It seems that in samples prepared in air the ratio $R(P_{O_2}; T) = M^{n+4}/M^{n+3}$ is controlled by the partial oxygen pressure. When these samples are cooled slowly during the final preparation step the $R(P_{O_2}; T)$ is different from the nominal Ca concentration, $R_x = x/(1-x)$.

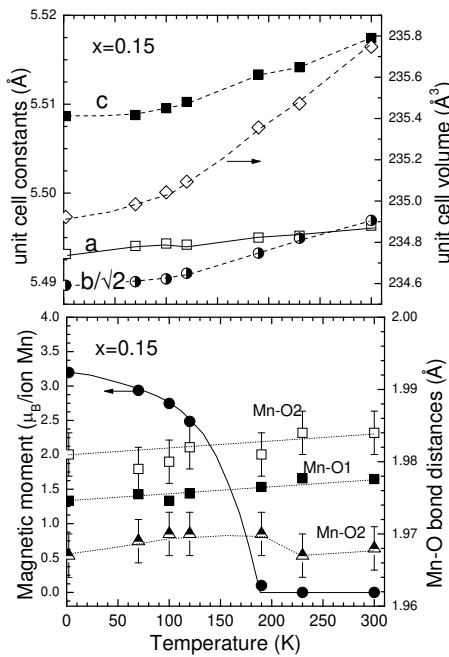


FIG. 14: (upper panel) Temperature variation of the lattice parameters and unit-cell volume for $\text{La}_{0.85}\text{Ca}_{0.15}\text{MnO}_3$ compound prepared in air atmosphere. (lower panel) Temperature variation of the ordered ferromagnetic moment and Mn-O₁ bond lengths. Lines through the experimental points are guides to the eye.

In order to maintain electric charge neutrality, cation vacancies are created. This effect is significant for $x < 0.2$. Therefore, in order to produce stoichiometric samples we must use reduced atmosphere conditions or quench the sample from high temperature to liquid N₂.^{9,10,11} The presence of cation vacancies completely destroys the coherent JT distortion even for the $x = 0$ sample.⁹ In the cation deficient samples firstly, it seems that the $\text{R} = \text{Mn}^{+4} = \text{Mn}^{+3}$ is locked to a nearly independent x value, and secondly the M^{\pm} phase which

concerns a coherent JT distortion cannot be formed due to the cation vacancies. In this context numerous experimental results in the particular Ca regime should be interpreted. It is a mystery why the cation deficient samples show similar bulk magnetic measurements near $T = 100$ K as the stoichiometric ones. The stoichiometric samples display a structural transition at $T_{\text{M}^{\pm}\text{M}^{\pm}}$, therefore it is reasonable to correlate this anomaly with the particular shape of the curves obtained in dc magnetic and ac-susceptibility measurements. For non stoichiometric samples such structural anomaly is absent leaving open the question about the relation of the bulk magnetization anomaly among the two families of samples.

Summarizing, the crystal structure remnants, from stoichiometric samples of the $\text{La}_{1-x}\text{Ca}_x\text{MnO}_3$ compound in the FM I regime, are presented. All the samples ($0.11 \leq x \leq 0.175$) undergo a structural transition from O^{\pm} to M^{\pm} structure at T_{JT} . High resolution x-ray diffraction data revealed that for $T < T_{\text{JT}}$, $\text{La}_{1-x}\text{Ca}_x\text{MnO}_3$ compounds ($0.11 \leq x \leq 0.175$) have monoclinic $P\bar{2}_1/c$ symmetry. The major structural characteristic of this model is the two Mn sites. As the bond lengths are concerned the Mn2 site displays properties similar with those of the Mn site of the LaMnO_3 compound, while the Mn1 site, resembles the Mn site in the FM M regime. By further cooling, below the characteristic temperature $T_{\text{M}^{\pm}\text{M}^{\pm}}$, although, the structure remains the same, a strong reduction of the strain parameter $s = (a - c)/(a + c)$ is observed. This change has been accompanied by significant reduction of the monoclinic angle and is correlated with distinct changes in dc and ac magnetic measurements.

Acknowledgments

This work was partially supported from EU through the CHRX-CT 93-0116 access to large-scale facilities project.

* Author to whom correspondence should be addressed.
email: mpissas@imstem.okritos.gr

¹ D. Khomskii and G. Sawatzky, Solid State Comm. 102, 87 (1997).

² L. Pincard, J. Rodriguez-Carvajal, A. H. Moudden, A. Aanne, A. Revcolevschi, C. Dupas, Physica B 234-236, 856 (1997).

³ Y. Endoh, K. Hirota, S. Ishihara, S. Okamoto, Y. Murokami, A. Nishizawa, T. Fukuda, H. Kimura, H. Nojiri, K. Kaneko, and S. Maekawa, Phys. Rev. Lett. 82, 4328 (1999).

⁴ Y. Yamada, J. Suzuki, K. Oikawa, S. Katano, J. A. Fernandez-Baca, Phys. Rev. B 62, 11600 (2000).

⁵ A. M. Glazer, Acta Cryst. B 28, 3384 (1972); A. M. Glazer, Acta Cryst. A 31, 756 (1975); C. J. Howard and H. T. Stokes, Acta Cryst. B 54, 782 (1998); P. M. Woodward,

Acta Cryst. B 53, 32 (1997); P. M. Woodward, Acta Cryst. B 53, 44 (1997).

⁶ As the present study reveals that the true structure below the T_{JT} is monoclinic, we prefer to keep the symbols O^{\pm} and O^{++} in order to help the reader to compare our results with those of other studies.

⁷ J. Kanamori, J. Appl. Phys. 31, 14S (1960).

⁸ K. I. Kugel' and D. I. Khomskii, Sov. Phys. Uspekhi 25, 231 (1982).

⁹ M. Pissas and G. Papavassiliou J. Phys.: Condens. Matter 16, 6527 (2004).

¹⁰ B. Dobrowski, R. Dybinski, Z. Bokowski, and O. Chmaissem, J. Solid State. Chem. 146 448, (1999).

¹¹ J. A. M. van Roosmalen, E. H. P. Cordfuke, E. B. Heimholdt and H. W. Zandbergen, J. Solid State. Chem. 146 448, (1999).

¹² J. Rodriguez-Carvajal, *Physica B* 192, 55 (1993).

¹³ B. H. Toby, *J. Appl. Cryst.* 34, 210 (2001).

¹⁴ A. C. Larson and R. B. Von Dreele, *General Structure Analysis System (GSAS)*, Los Alamos National Laboratory Report LAUR 86-748 (2000).

¹⁵ L. W. Finger, D. E. Cox, A. P. Jephcoat, *J. Appl. Cryst.* 27, 892 (1994).

¹⁶ G. Biotteau, M. Hennion, F. Mousset, J. Rodriguez-Carvajal, L. Pinsard, A. Revcolevschi, Y. M. Mukovskii, and D. Shulyatev, *Phys. Rev. B* 64, 104421 (2001).

¹⁷ J. Rodriguez-Carvajal, M. Hennion, F. Mousset, A. H. Moudeden, L. Pinsard and A. Revcolevschi, *Phys. Rev. B* 57, R3189, (1998).

¹⁸ D. E. Cox, T. Iglesias, and E. Moshopoulou, K. Hirota, K. Takahashi, and Y. Endoh, *Phys. Rev. B* 64, 024431 (2001).

¹⁹ P. W. Stephens, *J. Appl. Cryst.*, 32, 281 (1999).

²⁰ M. J. Calderon, A. J. M. illis, K. H. Ahn, *Phys. Rev. B*, 68 100401(R) (2003).

²¹ K. H. Ahn, T. Lookman and A. R. Bishop, *Nature*, 428, 401 (2004).

²² P. G. Radaelli, D. E. Cox, M. Marezio and S-W. Cheong, *Phys. Rev. B* 55, 3015 (1997); P. G. Radaelli, G. Iannone, M. Marezio, H. Y. Hwang, S-W. Cheong, J. D. Jorgensen, D. N. Argyriou, *Phys. Rev. B* 56, 8265 (1997).

²³ J. Nogues, Vassil Skumryev, J. S. Muroz, B. Martínez, J. Fontcuberta, L. Pinsard and A. Revcolevschi, *Phys. Rev. B* 64, 024434 (2001).

²⁴ H. Nojiri, K. Kaneko, M. M. otokawa, K. Hirota, Y. Endoh, K. Takahashi, *Phys. Rev. B* 60, 4142 (1999). 980-8578,

²⁵ F. Mousset, M. Hennion, J. Rodriguez-Carvajal, H. Moudeden, L. Pinsard and A. Revcolevschi, *Phys. Rev. B* 54, 15149 (1996); Q. Huang, A. Santoro, J. W. Lynn, R. W. Erwin, J. A. Borchers, J. L. Peng and R. L. Greene, *Phys. Rev.* 55, 14987 (1997).

²⁶ V. M. Arkovich, E. Rozenberg, A. I. Shames, G. Gorodetsky, I. Fita, K. Suzuki, R. Puzniak, D. A. Shulyatev and Ya. M. Mukovskii, *Phys. Rev. B* 65, 144402 (2002).

²⁷ M. Pissas, G. Papavassiliou, E. Devlin, A. Simopoulos, V. Likodimos, cont-m at/0403446.

²⁸ G. Papavassiliou, M. Pissas, M. Belesi, M. Fardis, J. D. olin-sek, C. D. in itropoulos, and J. P. Ansermet, *Phys. Rev. Lett.* 91, 147205 (2003).

²⁹ M. V. Lobanov, A. M. Balagurov, V. Ju. Pomjakushin, P. Fischer, M. Gutmann, A. M. Abakumov, O. G. Dyachenko, E. V. Antipov, O. I. Lebedev, and G. Van Tendeloo, *Phys. Rev. B*, 61, 8941 (2000).

³⁰ B. Dabrowski, X. Xiong, Z. Bokowski, R. Dabrowski, P. W. Klamut, J. E. Siewenie, O. Chmaissem, J. Schaefer, C. W. Kimball, J. D. Jorgensen and S. Short, *Phys. Rev. B* 60, 7006 (1999).

³¹ X. Xiong, B. Dabrowski, O. Chmaissem, Z. Bokowski, S. Kolesnik, R. Dabrowski, C. W. Kimball, and J. D. Jorgensen, *Phys. Rev. B* 60, 10186 (1999).

³² J. Eck, P. Wochner, D. Bruns, B. Buchner, U. Gebhardt, S. Kiele, P. Reutler, and A. Revcolevschi, *Phys. Rev. B* 69, 104413 (2003).

³³ T. Mizokawa, D. I. Khomskii, and G. A. Sawatzky, *Phys. Rev. B* 61, R3776 (2000).

³⁴ R. Kilian and G. Khaliullin, *Phys. Rev. B* 58, 11841(R) (1998).

³⁵ Q. Huang, A. Santoro, J. W. Lynn, R. W. Erwin, J. A. Borchers, J. L. Peng, K. Gosh and R. L. Greene, *Phys. Rev. B* 58, 2684 (1998); Q. Huang, A. Santoro, J. W. Lynn, R. W. Erwin, J. A. Borchers, J. L. Peng, and R. L. Greene, *Phys. Rev. B* 55, 14987 (1998); J. W. Lynn, R. W. Erwin, J. A. Borchers, Q. Huang, A. Santoro, J. L. Peng and Z. Y. Li, *Phys. Rev. Lett.* 76, 4046 (1996).

³⁶ P. Dai, J. Zhang, H. A. Mook, S.-H. Liou, P. A. Dowben, E. W. Plummer, *Phys. Rev. B* 54, R3694, (1996).

³⁷ P. Dai, J. Zhang, H. A. Mook, F. Foong, S.-H. Liou, P. A. Dowben and E. W. Plummer, *Sol. St. Comm.* 100, 865 (1996).

³⁸ P. A. Algarabel, J. M. De Teresa, J. B. Lasco, M. R. Ibarra, C. Z. Kapusta, M. Sikora, D. Zajac, P. C. Riedi and C. Ritter, *Phys. Rev. B* 67, 134402 (2003).